ACS APPLIED MATERIALS & INTERFACES

www.acsami.org

Forum Article

Redox-Active High-Performance Polyimides as Versatile Electrode Materials for Organic Lithium- and Sodium-Ion Batteries

Andre Lammiduk Lubis, Febri Baskoro, Ting-Hsuan Lin, Hui Qi Wong, Guey-Sheng Liou,* and Hung-Ju Yen*

Cite This: https://doi.org/10.1021/acsami.3c10722

Read Online

ACCESS | Metrics & More | Article Recommendations | Supporting Information

ABSTRACT: Organic electrode materials for rechargeable batteries show great promise for improving the storage capacity, reducing production costs, and minimizing environmental impact toward sustainability. In this study, we report a series of newly synthesized arylamine-based polyimides, TPPA-PIs, with three different bridge functionalizations on the imide rings and isomeric constituents that can work as versatile battery electrodes. As a lithium-ion battery cathode, a maximum energy density of 248 Wh kg^{-1} with high voltage operation up to 4.0 V can be achieved. As a lithium-ion battery anode, the TPPA-PIs showed a reversible storage capacity of 806 mA h g^{-1} at 100 mA g^{-1} current density with good rate capability up to a current density of 2000 mA g^{-1}. Moreover, when applied as sodium-ion battery anodes, TPPA-PIs delivered an optimum specific capacity of up to 218 mA h g^{-1} after 50 cycles at a 50 mA g^{-1} current density and revealed a long cycling stability up to 1000 cycles under a high current density of 1000 mA g^{-1}. More importantly, these electrochemical performances of TPPA-PIs are among the best compared with other reported polymer-based electrodes. The mechanistic studies show that both bridge functionalization on the imide units and isomerism impact the electrochemical performance by regulating their intrinsic properties such as charge storage behavior, ion diffusivity, and activation energy. We believe that such a detailed study of the structural design to electrochemical performance of these polymeric electrodes will offer insights into materials development and optimization for next-generation multifunctional energy storage devices in a wide range of applications.

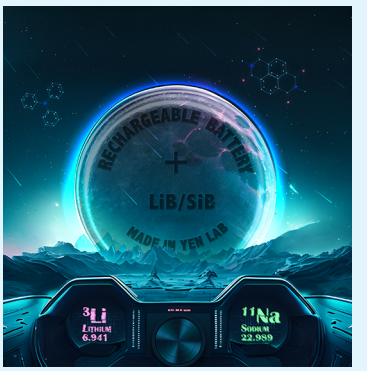

KEYWORDS: *Polyimide, Arylamine, Organic electrode, Lithium-ion battery, Sodium-ion battery*

INTRODUCTION

Lithium-ion batteries (LiBs) have long been commercialized as energy storage devices ranging from portable electronics to energy stations due to their advantages such as light weight, high power and energy density, and fast charging capability.[1−5] However, LiBs face various problems associated with the use of inorganic materials, such as limited resources, high cost, and environmental concerns.[6−10] In this particular interest, organic-based electrode materials have sparked a new research interest in LiB electrode development due to their tunable structural design, tunable redox properties, low cost, environmental friendliness, and sustainability.[11−18] Among the organic-based electrode materials, carbonyl-based species have been explored as an alternative because of their high theoretical capacities, structural diversity, and excellent electrochemical performance.[19−23] Unfortunately, these carbonyl-based compounds faced high solubility in organic electrolytes and limited electrical conductivity.[14,24−26] To improve the material stability of the carbonyl-based compounds, polymerization has been seen as a promising strategy.[23,27−31]

Aromatic polyimides (PIs) are well-known for their superior thermal stability, mechanical characteristics, and chemical stability.[32,33] As redox-active materials, the PIs have been intensively studied as LiB electrode materials because their redox-active carbonyl groups could store Li ions via a two-electron-transfer reaction.[21,23] Compared with their small molecular imide units, PIs showed significantly improved material stability during the electrochemical process. However, it often results in low specific capacity due to the electrochemical inert unit in the polymeric backbone.[23,31,32] Therefore, electroactive moieties could be further introduced in the PIs to improve their electrochemical performances during cycling. Previous studies have reported that tetracarboxylic anhydride based PIs, such as pyromellitic dianhydride (PMDA) and 1,4,5,8-naphthalenetetracarboxylic dianhydride (NTCDA), demonstrated electrochemical capability as LiB electrodes.[21,30,34] He *et al.* employed PMDA-based PI as LiB anode and discovered that the as-synthesized PMDA-based PI anode delivered a specific capacity of 832 mA h g^{-1} at the

Special Issue: Organic Battery Materials

Received: July 21, 2023
Revised: November 27, 2023
Accepted: December 8, 2023

Scheme 1. Synthesis of TPPA-PIs by Two-Step Chemical Imidization

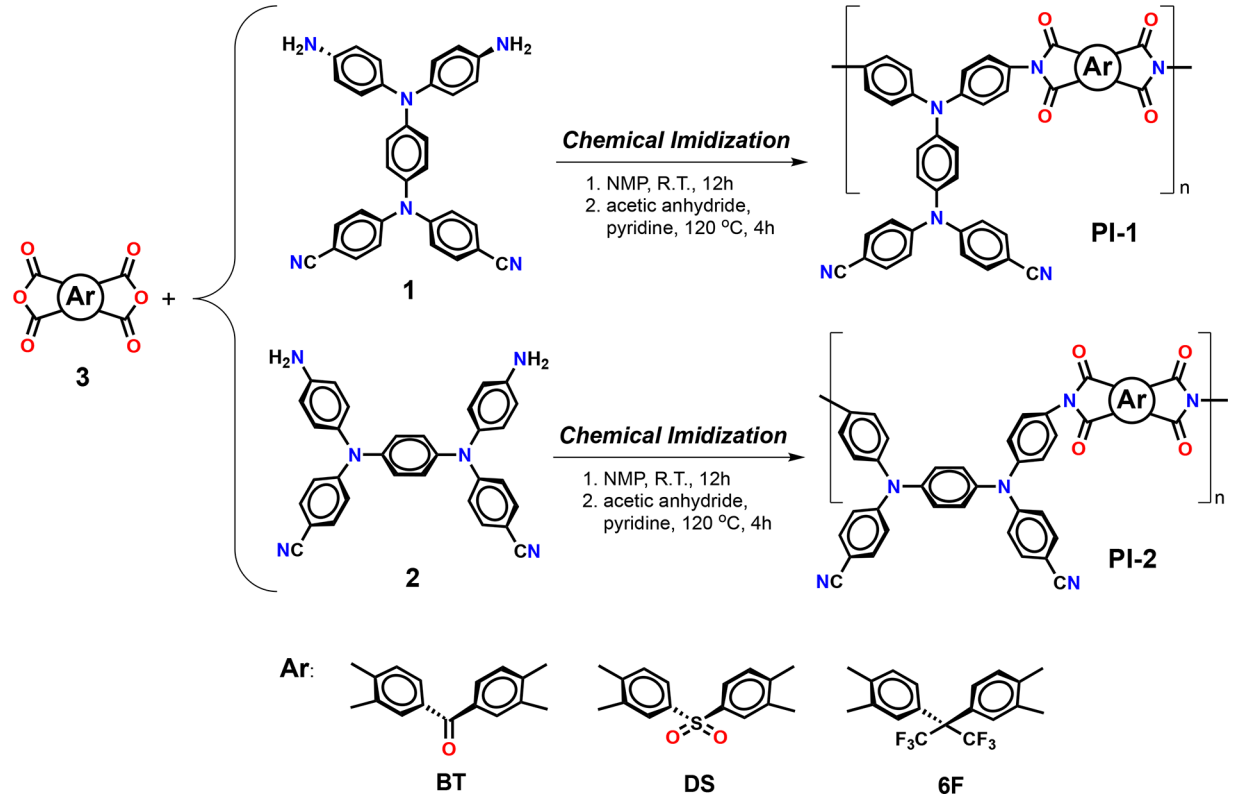

initial cycle. However, this capacity continuously dropped up to 50 cycles due to material instability.[35] Additionally, Zhang *et al.* reported that NTCDA-based PI could deliver a high capacity of ~150 mA h g^{-1} up to 70 cycles as LiB cathode material.[36] Several strategic structural designs could be employed to gain the optimum electrochemical performance of PI-based electrodes.[37] Song et al. found that PMDA- and NTCDA-based PIs delivered a distinct electrochemical behavior by adjusting the molecular structure.[21] In addition, different conformational structures (isomerism) have also been found to impact the electrochemical characters of PI-based anodes.[37]

In addition, triphenylamine (TPA)-based polymers have been recently investigated as potential candidates for LiB electrode materials due to their reversible, fast, and stable radical redox reaction.[31,38] As LiB cathode, TPA-based polymers have been reported to have a high voltage operation (~3.6 V) and cycling stability.[39−41] The charging and discharging process of the TPA-based electrode is accomplished by the doping and dedoping process of PF_6^- species into radical nitrogen.[42] However, the theoretical capacity of TPA-based polymers has been reported to be relatively low (109 mA h g^{-1}), which limits their practical application.[39,43] Strategically, the theoretical capacity of the TPA-based polymers can be improved by increasing the ratio of electrons transferred in each repeating unit. Of particular interest, the TPA-based derivative *N,N,N′,N′*-tetraphenyl-1,4-benzenediamine (TPPA) has popped out. TPPA has been known to have a structure similar to that of TPA but with a higher free radical density than that of TPA-based molecules, thus enabling its potential as an electrode material with multi-electron transfer.[31,44,45] Nevertheless, the expensive catalyst needed for the synthesis, long-term cyclability, and solubility of the organic radical polymers in electrolytes still hindered their application.[45] Motivated by our previous study, the TPPA unit can be incorporated in the PI backbone via a one-step imidization process, resulting in a hybrid polymer with outstanding cycling stability.[31] Therefore, inspired by these literature sources, it would be interesting to evaluate the TPPA-PI-based polymers with different functionalities and structures to optimize their battery performance.

Herein, we report a series of newly synthesized TPPA-PIs with three different bridge functionalizations on imide rings and their isomeric constituents, namely **PIBT-1**, **PIBT-2**, **PIDS-1**, **PIDS-2**, **PI6F-1**, and **PI6F-2**, as battery electrode materials. In this hybrid polymer design, a cyano functional group has been included in the TPPA backbone to elevate the lowest unoccupied molecular orbital (LUMO) energy level; as a result, the reduction voltage and energy density can be increased.[21] The result shows that the as-synthesized TPPA-PI cathodes delivered a high energy density of ~248 Wh kg^{-1} up to 100 cycles at 50 mA g^{-1} and exhibited long cycling stability up to 1000 charge/discharge processes under a high current density of 1000 mA g^{-1}. As an anode, the specific capacity of ~806 mA h g^{-1} can be stored after 100 cycles under the current density of 100 mA g^{-1}. Furthermore, the systematic mechanistic studies show that different bridge functionalizations on the imide unit and isomerism impact the ionic diffusion, charge storage characteristics, and activation energy of battery electrode materials. Our study shines a way to the strategically structural design of polymeric electrodes for next-generation organic batteries.

RESULTS AND DISCUSSION

Polymer Synthesis and Characterization. Two series of TPPA-based PIs were prepared by the reaction of diamines **1**

https://doi.org/10.1021/acsami.3c10722
ACS Appl. Mater. Interfaces XXXX, XXX, XXX−XXX

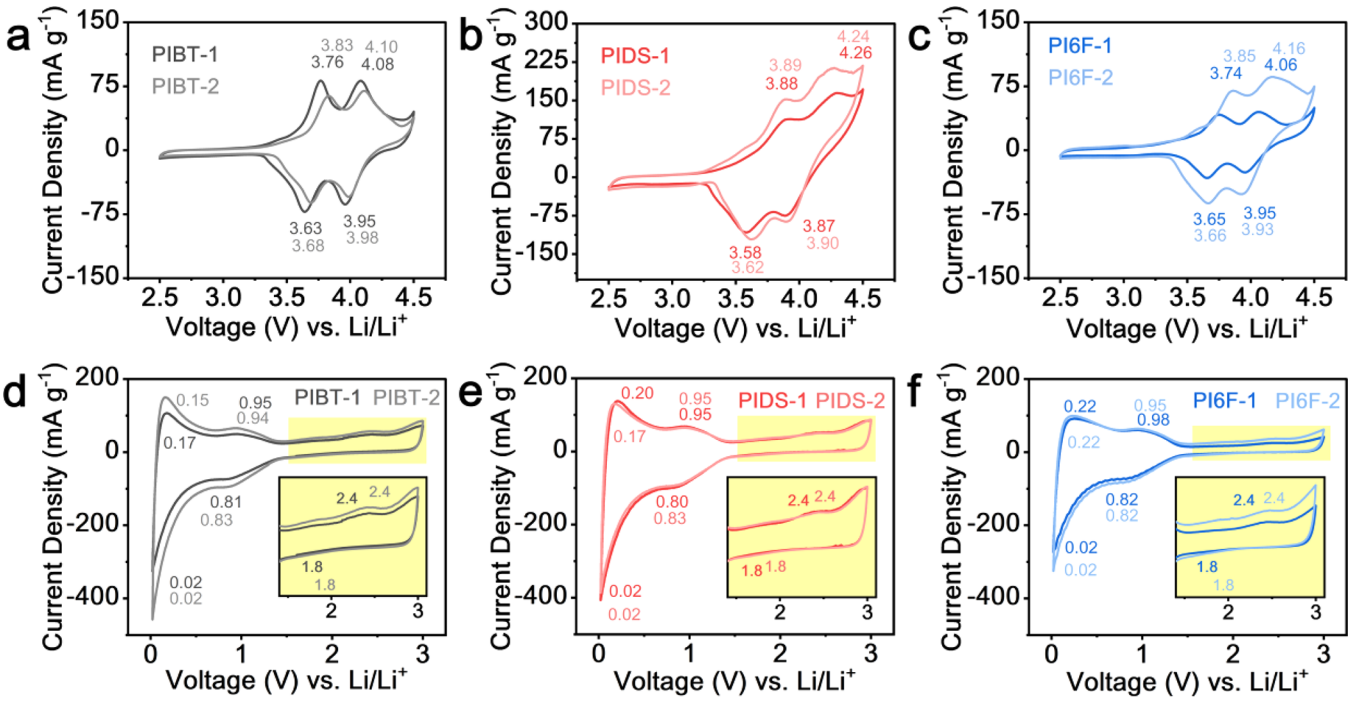

Figure 1. Cyclic voltammogram of TPPA-PIs as both LiB (a–c) cathodes and (d–f) anodes.

and **2** with three commercially available dianhydrides in *N*-methylpyrrolidone (NMP) at room temperature to form the precursor poly(amic acid)s, followed by chemical imidization (Scheme 1). In the first step, the viscosities of the reaction mixtures became very high as poly(amic acid)s were formed, indicating the formation of high molecular weight polymers. The poly(amic acid) precursors could be chemically dehydrated to PIs by treatment with acetic anhydride and pyridine and could afford flexible and tough films. All the polymerization reactions proceeded homogeneously and led to the highly viscous polymer solutions as well as a tough fiberlike form when the resulting polymer solutions were slowly poured into methanol. The reaction yields, molecular weights, and elemental analyses of the obtained PIs are tabulated in Table S1 to confirm the completion of polymerization. In addition, the inherent viscosities of these PIs are summarized in Table S2, and the formation of PIs was confirmed by IR and NMR spectroscopic techniques. As shown in Figure S1, the typical N–H stretching of diamines **1** and **2** was found to disappear after the imidization process, depicting vibrational spectra of C≡N stretching and asymmetric and symmetric C═O stretching of TPPA-PIs at 2222, 1723–1676, and 1608–1597 cm^{-1}, respectively. This indicates a successful polymerization process. Meanwhile, the absorption bands of −S═O and $-CF_3$ for the **PIDS** and **PI6F** polymers are observed at 1319 and 1210 cm^{-1}, respectively. Figures S2–S6 show the NMR spectra of synthesized PIs in $CDCl_3$ or DMSO-d_6, where the spectrum agrees well with the proposed molecular structure. In addition, the model compounds **BTDA2+**, **DSDA2+**, and **6FDA2+** were synthesized from the condensation of a monoamine 4-*tert*-butylaniline with three dianhydrides, as shown in Scheme S1, to verify the electrochemical behavior of imide moieties clearly. The NMR spectroscopic analyses shown in Figure S7 suggest the successful preparation of the target model compounds. Additionally, the powder X-ray diffraction spectroscopy (PXRD) measurement and N_2 adsorption study are performed to evaluate the physical properties of the TPPA-PIs. As depicted in Figure S8, a broad spectrum is monitored for all TPPA-PIs with a small diffraction peak at ∼22.6°, indicating a highly amorphous structure. Furthermore, the crystallinity analysis on the diffraction peak at ∼22.6° reveals that the degrees of crystallinity of TPPA-PIs were ∼9.41, 12.54, 10.84, 21.70, 11.99, and 12.74% for **PIBT-1**, **PIBT-2**, **PIDS-1**, **PIDS-2**, **PI6F-1**, and **PI6F-2**, respectively. This indicates that the TPPA-PI with the diamine **1** has a slightly higher amorphous region than that of with diamine **2**, which is possibly beneficial for facilitating faster Li^+ mobility. Moreover, the Brunauer–Emmett–Teller (BET) measurement (Figure S9) shows that the as-synthesized TPPA-PIs exhibited type II adsorption–desorption isotherms with N_2 adsorption capabilities of 121.90, 94.42, 127.17, 53.54, 83.59, and 81.09 $cm^3\ g^{-1}$ at 77 K for **PIBT-1**, **PIBT-2**, **PIDS-1**, **PIDS-2**, **PI6F-1**, and **PI6F-2**, respectively. The BET analysis also reveals that the TPPA-PIs exhibited BET surface areas of 68.29, 53.74, 58.09, 37.59, 56.04, and 51.31 $m^2\ g^{-1}$ for **PIBT-1**, **PIBT-2**, **PIDS-1**, **PIDS-2**, **PI6F-1**, and **PI6F-2**, respectively. This further suggests that the higher amorphous region of TPPA-PIs with diamine **1** leads to have a higher N_2 uptake and BET surface area, which could potentially enhance the Li^+ mobility. Furthermore, the Barrett–Joyner–Halenda (BJH) pore size distribution confirmed that the TPPA-PIs were dominated by the formation of mesopores (2–50 nm) and macropores (>50 nm) (Figure S9).

The solubility behaviors of polymers obtained by chemical imidization were investigated qualitatively, and the results are listed in Table S2. The solubility behaviors of the PIs depended on their chain-packing abilities and intermolecular interactions that were affected by the rigidity, symmetry, and regularity of the molecular backbone. These PIs exhibited higher solubilities in polar aprotic organic solvents such as NMP, *N*,*N*-dimethylacetamide (DMAc), *N*,*N*-dimethylformamide (DMF), dimethyl sulfoxide (DMSO), and *m*-cresol. The

https://doi.org/10.1021/acsami.3c10722
ACS Appl. Mater. Interfaces XXXX, XXX, XXX–XXX

Scheme 2. Schematic Reaction Mechanism of the Representative TPPA-PI Cathodes: (a) PIBT-1; (b) PIBT-2; (c) PIDS-2; (d) PI6F-2

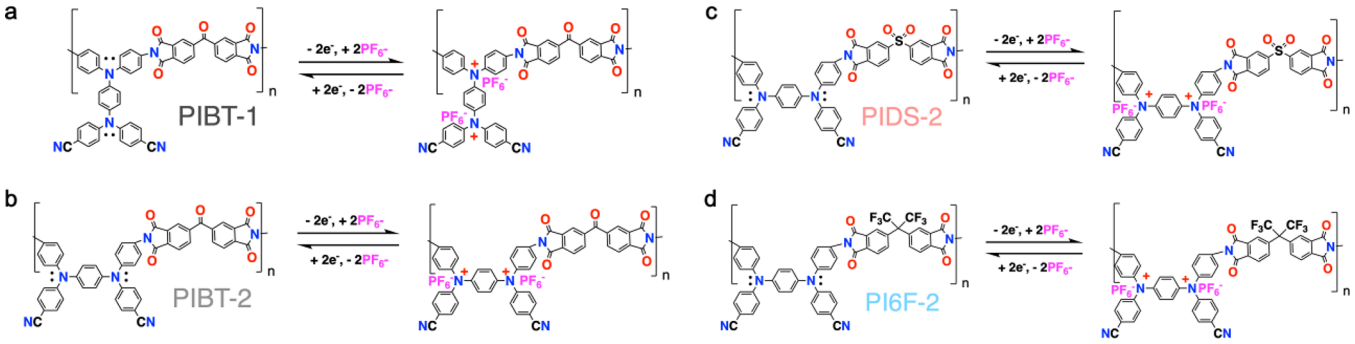

PIs **PI6F-1** and **PI6F-2** were soluble in polar aprotic organic solvents and less polar solvents such as tetrahydrofuran (THF) and $CHCl_3$. The excellent solubility can be attributable to the hexafluoroisopropylidene structure, which limits the charge transfer complex formation and reduces the intermolecular interactions. The thermal properties of these PIs are summarized in Table S3. All of the PIs exhibited similar thermogravimetric analysis (TGA) patterns with no significant weight loss below 450 °C in air or in a nitrogen atmosphere. The 10% weight loss temperatures of the polymers in nitrogen and air were recorded in the ranges 570−650 and 580−645 °C, respectively. The carbonized residue (char yield) of these polymers in the nitrogen atmosphere was more than 64% at 800 °C. The high char yields of these polymers can be ascribed to their high aromatic contents.

Redox Properties of TPPA-PI Electrodes. Cyclic voltammetry (CV) measurements were first applied to investigate the redox capabilities of TPPA-PIs as LiB electrodes. Figure 1a−c depicts the CV curves of TPPA-PI cathodes with their corresponding structural isomers, with the voltage ranging from 2.5 to 4.5 V (vs Li/Li^+) under a scan rate of 0.2 mV s^{-1}. As shown in Figure 1a, **PIBT**-based polymers generated two pairs of redox peaks at 3.63/3.76 and 3.95/4.08 V, which correlated with the PF_6^- anion doped and dedoped process on the two radical nitrogen atoms of diamine units, respectively.[36,39] The first redox couple at 3.63/3.76 V is ascribed to the first radical cation during the p-type doping process; another redox couple at a higher potential of 3.95/4.08 V is related to the reaction of the second radical cation.[31,39] Additionally, the **PIDS**- and **PI6F**-based polymers exhibited a typically similar behavior of two pair redox peaks at ∼3.6/3.7 and ∼3.9/4.08 V (Figure 1b,c). This electrochemical behavior confirmed the redox activity of the TPPA unit via multielectron reaction on the two radical cations of nitrogen atoms during the charge/discharge process. Notably, **PI6F-2** has a higher intensity than that of **PI6F-1** (Figure 1c), which can be ascribed to the different structural conformation and strong electron-withdrawing functionalization ($-CF_3$) on **PI6F** polymers. The strong electron-withdrawing group of $-CF_3$ significantly impacts the electron density of **PI6F-1**, thus considerably reducing the current density during the electrochemical process. Notably, the high oxidation potential of newly synthesized TPPA-PIs up to ∼4.08 V will be beneficial to achieving higher energy density batteries since the cutoff voltage is one of the critical parameters used to define energy density (energy density (Wh kg^{-1}) = capacity (C) × voltage (V)).[45]

To further investigate the capability of TPPA-PIs for LiB electrodes, the redox properties of anodes have also been evaluated in the potential range of 0.02−3.0 V (vs Li/Li^+) at 0.1 mV s^{-1} (Figure 1d−f). As shown in Figure 1d−f, all TPPA-PI anodes show identical CV characteristics with three redox pairs at ∼1.8/2.4, 0.81/0.95, and 0.02/0.17 V, depicting a successful lithiation/delithiation process. The first redox peak at ∼1.8/2.4 V could be attributed to the Li^+ attachment/detachment on the carbonyl groups of the diimide unit. The redox process at ∼0.81/0.95 V might be ascribed to the Li^+ attachment/detachment on the cyano group,[11] and the second redox behavior at 0.02/0.17 V is monitored for the lithiation/delithiation process on the carbonaceous groups.[46,47] Additionally, to verify the redox behavior of imide units in the TPPA-PIs, the electrochemistry of model compounds **BTDA2+**, **DSDA2+**, and **6FDA2+** was evaluated in the LiB half-cell for both anode and cathode. As depicted in Figure S10a−c, the CV curves of model compound anodes were markedly identical with those of the TPPA-PI anodes (Figure 1d−f), showing a redox peak at ∼1.8/2.4 V. Alternatively, two distinct redox peaks were monitored on the model compounds as cathodes (Figure S10d−f), suggesting the reduction mechanism of arylene diimides is similar to that of the pyromellitic moiety.[48] Notably, these redox peaks were varied with differing bridge functionality on the diimide units. As shown in Figure S10d, **BTDA2+** exhibited two pair redox peaks at 1.97/2.93 and 1.6/2.12 V vs Li/Li^+, while **DSDA2+** showed redox activity at 2.04/2.53 and 1.77/2.39 V (Figure S10e). **6FDA2+** exhibited redox activity at 1.91/2.85 and 1.68/2.46 V vs Li/Li^+ (Figure S10f). This further suggests that the bridge functionality plays an important role in the electrochemical behavior of diimide units. Importantly, compared with redox properties as cathodes, TPPA-PI anodes were not significantly influenced by structural conformation and bridge functionalization. In summary, the CV measurements confirmed the ability of applying TPPA-PIs as both battery cathode and anode materials.

Battery Performance of TPPA-PI LiB Cathodes. To probe the capability of TPPA-PI cathodes, the LiB half-cells were assembled and galvanostatically charged/discharged in a potential window of 2.5−4.5 V (vs Li/Li^+). Figure S11 shows the galvanostatic profiles of TPPA-PI cathodes at a current density of 50 mA g^{-1}. As depicted in Figure S11, two plateaus were monitored at the potentials of 3.76 and 4.08 V for all TPPA-PI cathodes, and the results were consistent with the CV curves in Figure 1. These plateaus can correspond to the successful doped and dedoped process of the PF_6^- anion to the radical nitrogen cation in TPPA units during the charge/

https://doi.org/10.1021/acsami.3c10722
ACS Appl. Mater. Interfaces XXXX, XXX, XXX−XXX

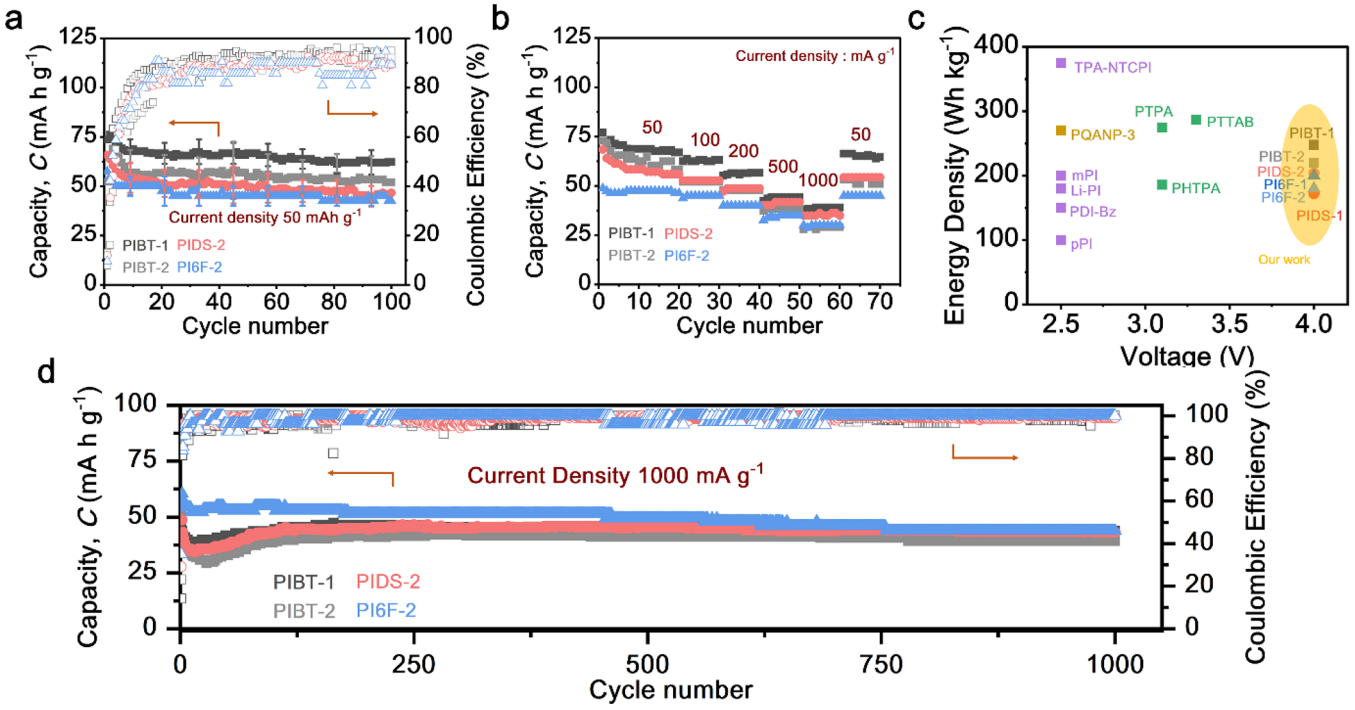

Figure 2. Electrochemical performance of TPPA-PI LiB cathodes. (a) Capacity profile at 50 mA g^{-1}. (b) Rate performance. (c) Energy density vs operating voltage. (d) Long cycling performance at 1000 mA g^{-1}.

discharge process. As shown in Figure S11, the series of **PIBT** cathodes have slightly higher capacities than those of **PIDS** and **PI6F** cathodes. The **PIBT-1** cathode showed an initial capacity of 85 mA h g^{-1}; the capacity gradually decreased to 62 mA h g^{-1} after 100 cycles (Figure S11a). This capacity was slightly higher than that of **PIBT-2** (54 mA h g^{-1}; Figure S11d), which could be ascribed to different structural conformations, thus impacting the ion transport properties of **PIBT**-based cathodes during the electrochemical process. In addition, the **PIDS**-based cathodes exhibited almost equal capacities of 45 and 48 mA h g^{-1} for **PIDS-1** and **PIDS-2**, respectively, after 100 cycles at 50 mA g^{-1} (Figure S11b,e). Meanwhile, the **PI6F**-based cathodes delivered capacities of 46.5 and 42.5 mA h g^{-1} for **PI6F-1** and **PI6F-2**, respectively, after 100 cycles at 50 mA g^{-1} (Figure S11c,f), indicating that electron-withdrawing groups ($-SO_2$ and $-CF_3$) on the imide unit impact the cathode performance. Scheme 2 represents the possible reaction mechanism of TPPA-PI cathodes during the charge−discharge process in a voltage range of 2.5−4.5 V. As shown in Scheme 2, two PF_6^- anions could be stored in TPPA units by two-electron transfer. This mechanism is indicated by symmetrical redox peaks around 3.6/3.7 and 3.9/4.08 V and is consistent with previous literature.[31,36]

Figure 2a depicts the capacity profiles of representative TPPA-PI cathodes at 50 mA g^{-1}, namely **PIBT-1**, **PIBT-2**, **PIDS-2**, and **PI6F-2**. As shown in Figure 2a, these PI cathodes could maintain their optimum performance and minimum capacity decay for up to 100 cycles under 50 mA g^{-1}. Notably, the **PIBT**-based cathodes have slightly higher capacities than those of **PIDS** and **PI6F** cathodes, which agrees with the galvanostatic profile (Figure S11). The **PIBT-1** cathode exhibited the highest capacity of 62 mA h g^{-1} with ∼95% Coulombic efficiency (CE) after 100 cycles (Figure 2a). The other cathodes, **PIBT-2**, **PIDS-2**, and **PI6F-2**, show stable capacities of 52, 48, and 44 mA h g^{-1}, respectively, after 100 cycles at 50 mA g^{-1}. Additionally, the areal capacities of TPPA-PIs have also been estimated to obtain a better understanding for practical application. As presented in Table S4, the **PIBT-1** cathode offered a higher areal capacity of 6.572 mA h m^{-2} among TPPA-PI cathodes. These results again confirmed that the structural conformation and bridge functionalization strongly impact the battery performance of TPPA-PI cathodes.

Additionally, the rate performance test has also been carried out for representative TPPA-PI cathodes to probe the rate capability under different current densities. As shown in Figure 2b, **PIBT-1** demonstrated specific capacities of 69, 63, 56.5, 44, and 39 mA h g^{-1} at current densities of 50, 100, 200, 500, and 1000 mA g^{-1}, respectively. Its isomer, **PIBT-2**, exhibited slightly lower capacities of 62.5, 52, 48, 38, and 29 mA h g^{-1} at 50, 100, 200, 500, and 1000 mA g^{-1} current densities. Furthermore, **PIDS-2** showed specific capacities of 58, 53, 49, 42, and 35 mA h g^{-1} at current densities of 50, 100, 200, 500, and 1000 mAh g^{-1}. The least specific capacities of 47.5, 45, 40, 35, and 30 mA h g^{-1} were obtained by **PI6F-2** under current densities of 50, 100, 200, 500, and 1000 mA g^{-1}, respectively. Notably, the remarkable rate capability is indicated by the optimum capacities of **PIBT-1** (65 mA h g^{-1}), **PIBT-2** (51 mA h g^{-1}), **PIDS-2** (54 mA h g^{-1}), and **PI6F-2** (45 mA h g^{-1}) that could be regained after the current density was switched back to 50 mA g^{-1}.

In addition, Figure 2c summarizes the energy density versus voltage plot of polymer-based LiB cathodes. As depicted in Figure 2c, our as-synthesized TPPA-PI cathodes have the highest operating voltages and comparable energy densities up to 248 Wh kg^{-1} for **PIBT-1**. A detailed comparison can also be seen in Table S5. Moreover, the long cycling performance showed that the TPPA-PI cathodes demonstrated excellent material stability, cycling stability, and reversibility for up to 1000 cycles at a high current density of 1000 mA g^{-1} (Figure 2d).

https://doi.org/10.1021/acsami.3c10722
ACS Appl. Mater. Interfaces XXXX, XXX, XXX−XXX

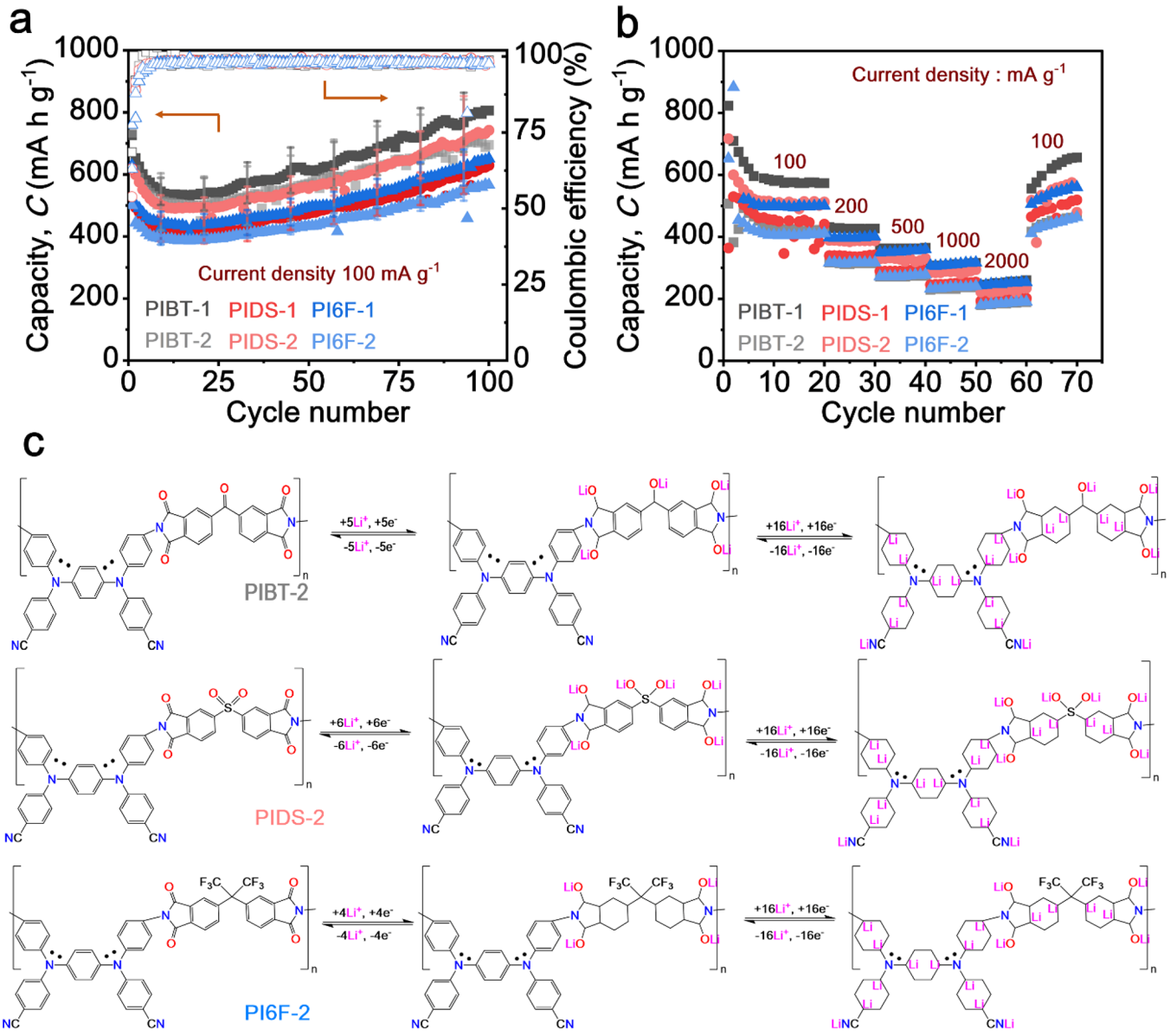

Figure 3. Electrochemical performance of TPPA-PI LiB anodes. (a) Capacity profile at 100 mA g^{-1}. (b) Rate performance. (c) Schematic reaction.

Battery Performance of TPPA-PI LiB Anodes. To investigate the capability of TTPA-PIs as LiB anodes, half-cells were prepared and cycled at potentials ranging from 0.02 to 3.0 V (vs Li/Li^+). As shown in Figure S12, the galvanostatic profiles of TPPA-PI anodes show unrecognizable redox plateaus at 0.8 and 0.02 V, depicting a sloping curve at the potentials of 0.02−3.0 V, suggesting a typical superlithiation process on the TPPA-PI anodes.[49,50] Furthermore, the irreversible capacity loss could be monitored for all TPPA-PI anodes at the first cycle due to the generation of solid−electrolyte interphase (SEI) layers.[51,52] Importantly, a gradual capacity increase can be observed for all TPPA-PI anodes during electrochemical cycling (Figure S12). This gradual capacity increase during cycling might be associated with the increasing Li^+ transfer throughout the cycling process and the activation period of TPPA-PI anodes to get all of the Li^+ binding sites fully lithiated.[14,30,49,53,54] This phenomenon of ascending capacity during cycling has also been reported previously for polymeric anodes.[11,46,55] Additionally, we carried out electrochemical impedance spectroscopy (EIS) before and after cycling (Figure S13) to probe the increasing Li^+ transport during cycling performance. The fitted parameters are summarized in Table S6. As shown in Figure S13 and Table S6, values of the charge transfer resistance (R_{ct}) of TPPA-PIs significantly dropped after 100 cycles, thus resulting in dramatically enhanced Li^+ diffusivity (D_{Li}). This suggests that enhanced Li^+ mobility during cycling plays a crucial role in the gradual increase of specific capacity during cycling. In good agreement with the galvanostatic profiles, the capacity profiles of TPPA-PI anodes depict a gradual capacity increase during electrochemical cycling (Figure 3a). As shown in Figure 3a, **PIBT-1** generated the highest specific capacity of 806 mA h g^{-1} after 100 cycles at 100 mA g^{-1}. Furthermore, the rest of the TPPA-PI anodes show optimum capacities of 719, 629, 742, 651, and 567 mA h g^{-1} after 100 cycles at 100 mA g^{-1} for **PIBT-2**, **PIDS-1**, **PIDS-2**, **PI6F-1**, and **PI6F-2**, respectively. Meanwhile, **PIBT-1** again shows the highest areal capacity of 51.584 mA h m^{-2} (Table S4), followed by **PIDS-2** (47.488 mA h m^{-2}), **PIBT-2** (46.016 mA h m^{-2}), **PI6F-1** (41.664 mA h m^{-2}), **PIDS-1** (40.256 mA h m^{-2}), and **PI6F-2** (36.288 mA h

https://doi.org/10.1021/acsami.3c10722
ACS Appl. Mater. Interfaces XXXX, XXX, XXX−XXX

m^{-2}), respectively. This electrochemical performance is among the best for polymeric battery anodes (Table S7). Moreover, to verify the high capacity of TPPA-PI anodes, half-cell LiBs consisting of **PIBT-1**, **PIBT-2**, **PIDS-2**, and **PI6F-2** anodes with higher active material contents have been fabricated (40 wt % active material, 50 wt % Super P, and 10 wt % PVDF). As depicted in Figure S14a, reducing the conductive carbon in the electrode while increasing the active material content results in significantly dropped capacity to ~450 mA h g^{-1} for **PIBT-1** and **PIBT-2** anodes under a low current density of 100 mA g^{-1}. Similarly, **PIDS-2** and **PI6F-2** also showed a lower capacity of ~100 mA h g^{-1} at 100 mA g^{-1}. The reduced capacity can also be observed in the long cycling test at 2000 mA g^{-1} (Figure S14b). This indicates that a higher conductive environment is necessary for the formation of superlithiation and fully utilized Li^+ binding sites in TPPA-PI anodes.

In addition, the TPPA-PI anodes also showed excellent rate capabilities up to 2000 mA g^{-1} (Figure 3b). As shown in Figure 3b, the **PIBT-1** anode exhibited specific capacities of 604, 427, 363, 311, and 256 mA h g^{-1} when the current density was varied from 100 mA g^{-1} to 200, 500, 1000, and 2000 mA g^{-1}, respectively. However, its conformational isomer, **PIBT-2**, delivered slightly lower capacities of 430, 315, 272.5, 232.5, and 185.2 mA h g^{-1} at 100, 200, 500, 1000, and 2000 mA g^{-1}, respectively, confirming that the structural conformation clearly affects the Li^+ storage capability. Additionally, **PIDS-1** delivered specific capacities of 455, 338, 290, 250, and 201 mA h g^{-1}, while **PIDS-2** showed specific capacities of 510, 388, 330, 287, and 229 mA h g^{-1} at 100, 200, 500, 1000, and 2000 mA g^{-1}, respectively. On the other hand, the **PI6F** series with a strong electron-withdrawing group ($-CF_3$) exhibited the lowest specific capacities of 500, 397, 351, 310, and 250 mA h g^{-1} for **PI6F-1** and 410, 317, 278, 238, and 186 mA h g^{-1} for **PI6F-2** at current densities of 100, 200, 500, 1000, and 2000 mA g^{-1}, respectively. This further suggests that different bridge functionalizations impact the storage capability. Notably, the outstanding rate capability of TPPA-PIs was confirmed by the optimum capacities of 610, 448, 491, 524, 538, and 442 mA h g^{-1} that could be recovered when the current density switched back to 100 mAg^{-1} for **PIBT-1**, **PIBT-2**, **PIDS-1**, **PIDS-2**, **PI6F-1**, and **PI6F-2**, respectively (Figure 3b).

Furthermore, battery full cells have been prepared to demonstrate the practical application of TPPA-PIs as LiB electrodes. LiB full cells have been fabricated by using **PIBT-1** as the cathode (40% active material) and **PIBT-1** as the anode (with active material percentages of 20 and 40%). Prior to the full cell assembly, the **PIBT-1** cathode and anode were first pretreated by being fully charged at 100 mA g^{-1}. As shown in Figure S15, the **PIBT-1** full cell delivered specific discharge capacities of ~93 mA h g^{-1} at 100 mA g^{-1} after 30 cycles and ~50 mA h g^{-1} at 1000 mA g^{-1} after 100 cycles. Notably, the electrochemical performance of the full cell shows that **PIBT-1** exhibited a similar capacity even with different active material percentages in the anode, indicating the compatibility of the TPPA-PI anode and cathode in the LiB full cell system.

To investigate the Li^+ storage mechanism in TPPA-PI anodes, ex situ FT-IR spectroscopy was used to monitor the functional group changes during the charge−discharge process. As depicted in Figure S16, the vibrational spectra of TPPA-PI anodes were observed closely to have similarities at the as-assembled stage (before cycling) and full discharge stages (delithiation at 3.0 V), depicting the vibrational mode of C≡N stretching (2222 cm^{-1}), symmetrical C═O stretching (~1720; 1670 cm^{-1}), and asymmetrical (~1610; 1590 cm^{-1}) C═O stretching. However, these spectra markedly differed from those at the full charge stages (lithiation at 0.02 V). The missing vibrational spectra of symmetrical and asymmetrical C═O stretching as well as C≡N stretching at the lithiation stage confirmed a successful Li^+ storage in TPPA-PI anodes. Additionally, a new vibrational spectrum of C═O from carbonate anions (CO_3^{2-}) was observed in both the lithiation and delithiation stages (Figure S16). This additional peak could be originated from electrolyte decomposition during SEI formation. Notably, the specific vibrational spectra of S═O on the **PIDS**-based anode at ~1310 cm^{-1} disappeared during the fully charged stage at 0.02 V (Figure S16c), indicating a successful lithiation process on the S═O group. On the other hand, the vibrational spectra of $-CF_3$ remain during the charge/discharge process, implying that the $-CF_3$ in the **PI6F**-based anode was not engaged in the Li^+ storage reaction (Figure S16d). Importantly, the recovered vibrational spectra of functional groups at the discharge stages further manifest the structural stability of TPPA-PI anodes during the electrochemical process.

In addition, it has been reported that the carbonaceous polymer has a unique Li^+ storage character, where each of the benzene rings in the polymer structures is able to reversibly receive six Li^+ ions during lithiation thus forming an Li_6C_6 complex rather than LiC_6 species.[56,57] Therefore, the Li^+ storage of TPPA-PI anodes was theoretically attributed to Li^+ insertion into C≡N, C═O, S═O, and carbonaceous sides. According to this theoretical assumption, **PIBT** and **PI6F** series could receive approximately 49 and 48 Li ions, respectively, while the **PIDS** series were estimated to accept 50 Li ions due to the additional S═O groups. Therefore, the theoretical capacity of TPPA-PI anodes can be estimated by

$$C\ (\text{mA h g}^{-1}) = \frac{nxF}{3.6M}$$

where C represents the theoretical capacity, n is the number of electrons involved, F is the Faraday constant (96 485 C mol^{-1}), and M is the molecular mass.[30,58,59] Therefore, the theoretical capacities of **PIBT**, **PIDS**, and **PI6F** series are estimated to be around 1855.9, 1839.6, and 1545.6 mA h g^{-1}, respectively. However, the cycling performance depicted that the TPPA-PI anodes with an optimum capacity only showed nearly 50% of their theoretical capacity (Figure 3a), suggesting a high energy barrier to fully optimize the Li^+ binding sites. Figure 3c shows the possible reaction of TPPA-PI anodes during the electrochemical process with two-step reactions occurring in the TPPA-PI anodes. First, two Li^+ ions were attached to the carbonyl functional groups during the first reduction via electron transfer. Second, Li^+ was further inserted into the cyano groups and aromatic rings of the TPPA-PI anodes.

Mechanistic Studies of TPPA-PI Electrodes. A series of measurements has been performed to investigate the effect of different bridge functionalizations in the TPPA-PIs on the electrochemical behavior as LiB electrodes. First, sweep rate CV analysis has been carried out to probe the charge storage behavior of TPPA-PIs as both cathode and anode. As for the cathode, sweep rate CV has been performed at potentials of 2.5−4.5 V under scan rates of 0.1−1.0 mV s^{-1} (Figure S17). As for the anode, the sweep rate CV study was performed at potentials of 0.02−3.0 V under scan rates of 0.1−1.0 mV s^{-1} (Figure S18). Further analysis of the total charge stored during

https://doi.org/10.1021/acsami.3c10722
ACS Appl. Mater. Interfaces XXXX, XXX, XXX−XXX

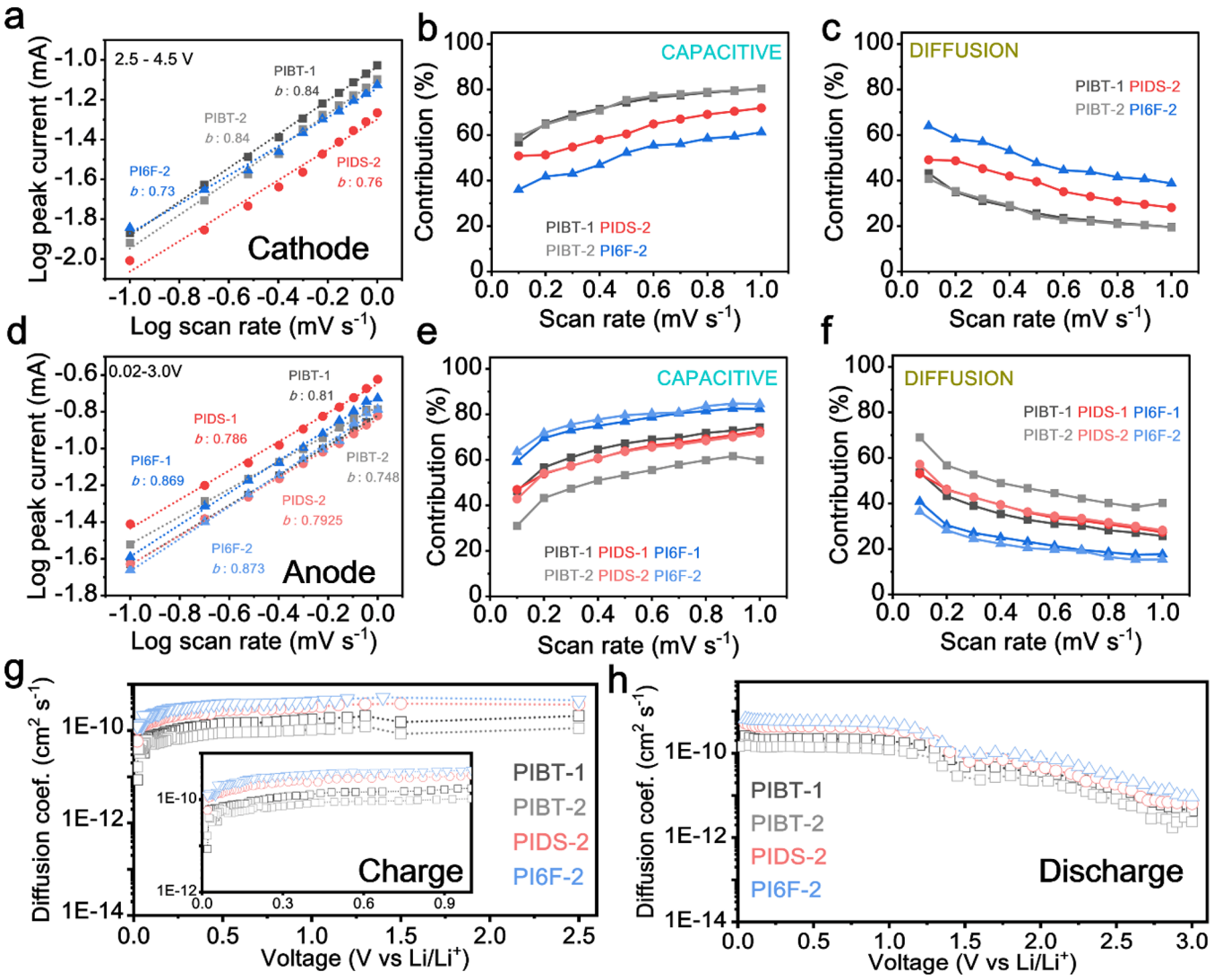

Figure 4. Mechanistic studies of TPPA-PI based electrode of LiB. Log peak current vs log scan rate plots and capacitive−diffusion contributions of TPPA-PI (a−c) cathode and (d−f) anode, respectively. (g and h) Ionic diffusion coefficient during charge and discharge processes, respectively.

the sweep rate CV showed that the *b*-value of **PIBT-1**, **PIBT-2**, **PIDS-2**, and **PI6F-2** ranged between 0.73 and 0.84 (Figure 4a), suggesting that the total charge stored on TPPA-PI cathodes was generated from the combination of diffusive and surface-controlled (capacitive) processes. In good agreement with results for the cathode, the *b*-value of TPPA-PIs was also found to range from 0.74 to 0.86 (Figure 4d), suggesting that synergic contribution of capacitive and diffusion processes played an important role. Notably, the TPPA-PI cathode and anode LiB shows a higher capacitive contribution (surface-controlled process), with the *b*-value falling up to 0.86, than the diffusion contribution. This higher capacitive contribution could be ascribed to the amorphous structure of TPPA-PIs (Figure S8). As shown in Figure S8, all TPPA-PIs were dominated by the amorphous structure with a degree of crystallinity of <21%. This low crystalline region in the TPPA-PIs offers more structural flexibility, thus significantly enhancing ion migration during the electrochemical process.[15,16,18]

In addition, to gain deep insight of the different bridge functionalizations to the charge storage characteristic in the TPPA-PIs electrodes, we carried out the quantitative analysis of capacitive ($k_1\nu$) and diffusion ($k_2\nu^{1/2}$) contributions from the slope and the intercept from the $i/\nu^{1/2}$ against $\nu^{1/2}$ plot for both TPPA-PI cathode and anode (Figure S19). As shown in Figure 4b,c, the capacitive contribution of TPPA-PI cathodes gradually increased as the scan rate varied from 0.1 to 1.0 mV s^{-1}, along with the decreasing trend in the diffusion contribution. Interestingly, the different conformations of the **PIBT-1** and **PIBT-2** cathodes were to be identical in the capacitive and diffusion contributions, indicating that isomerism did not impact the total charge storage behavior as a cathode. However, TPPA-PIs with electron-withdrawing groups (**PIDS** and **PI6F**) have significantly lower capacitive contributions than those of the **PIBT** series, along with much higher diffusion contributions (Figure 4b,c). This indicates that when we attached the electron-withdrawing groups in the TPPA-PI structure, the PF_6^- anions were forced to diffuse along the polymer backbone to overcome the energy barrier of charge polarization during the charge/discharge process, thus resulting in lower capacities of **PIDS** and **PI6F** cathodes than those of the **PIBT** series as cathode LiBs. Interestingly, this situation is inversed when the TPPA-PI is applied as anode LiB. As depicted in Figure 4e,f, the **PI6F** series anodes have the

https://doi.org/10.1021/acsami.3c10722
ACS Appl. Mater. Interfaces XXXX, XXX, XXX−XXX

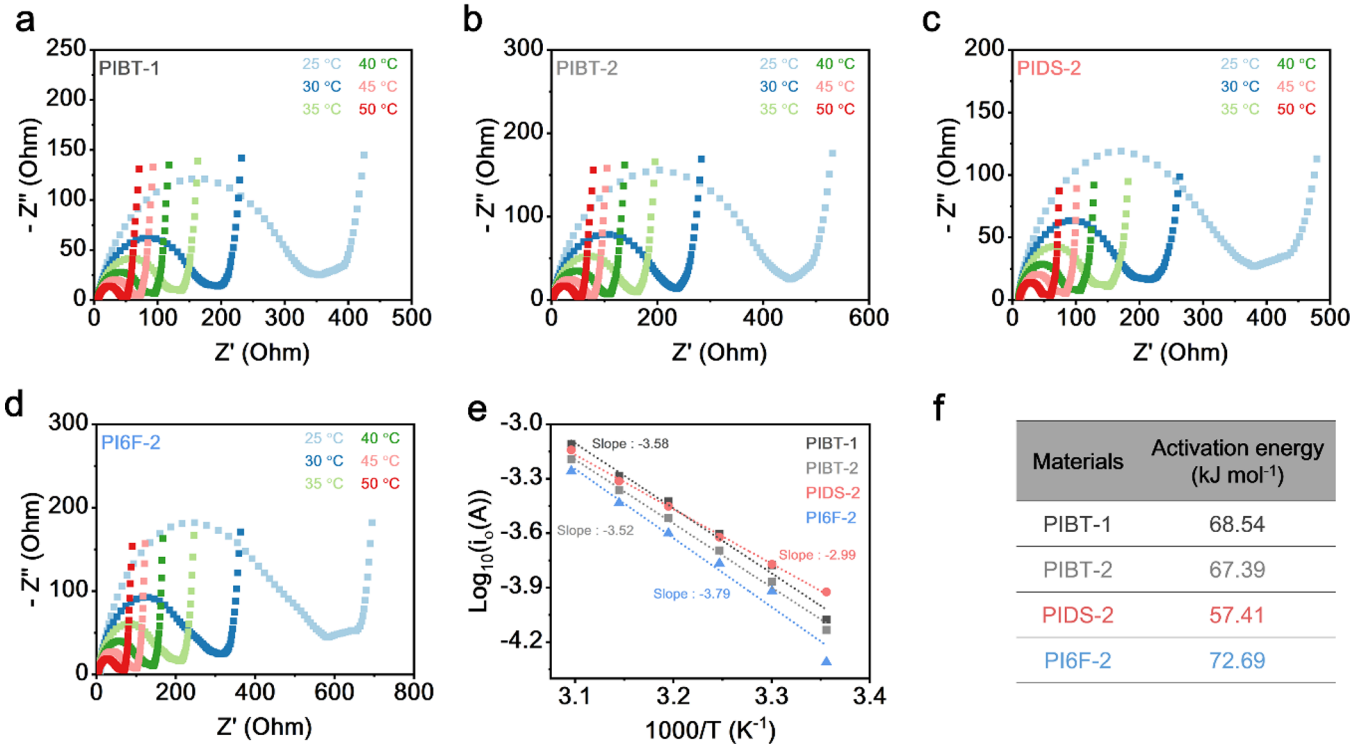

Materials	Activation energy (kJ mol^{-1})
PIBT-1	68.54
PIBT-2	67.39
PIDS-2	57.41
PI6F-2	72.69

Figure 5. Activation energy (E_a) calculation of TPPA-PIs. (a–d) Nyquist plots of **PIBT-1**, **PIBT-2**, **PIDS-2**, and **PI6F-2** at various temperatures. (e) Log i_0 vs 1000/T plot. (f) Calculated E_a's of TPPA-PI electrodes.

highest capacitive contributions and the lowest diffusion contributions compared with the rest of TPPA-PI anodes, followed by the **PIDS** series, **PIBT-1**, and **PIBT-2**. This further indicates that the bridge functionalization has a major role in the charge storage behavior of TPPA-PIs for both the cathode and anode. As cathode, the electron-withdrawing groups (O═S═O and $-CF_3$) increase the energy barrier of the PF_6^- anion to diffuse along the polymer backbone, thus significantly reducing the capacitive contribution in the TPPA-PI cathode. As for the anode, the higher electronegativities of the electron-withdrawing groups enhance the Li^+ adsorption on the TPPA-PI structure, therefore increasing the capacitive contribution. Meanwhile, isomerism has only a minimum effect on the TPPA-PIs compared with that of bridge functionalization. As shown in Figure 4e, **PIBT-1** has higher capacitive contribution than that of **PIBT-2**. This could be ascribed due to the higher surface area and lower crystalline region of **PIBT-1** (Figures S8 and S9), thus enhancing the ion migration. When the electron-withdrawing group was introduced via bridge functionalization on the imide unit, the isomerism effect on the charge storage characteristic was somewhat minimized for the **PIDS** and **PI6F** series (Figure 4e,f).

To further gain deep insight into the ionic diffusion in the TPPA-PI systems, the galvanostatic intermittent titration technique (GITT) was performed at 50 mA g^{-1} for representative TPPA-PI anodes. Figure S20 shows the typical galvanostatic profiles of the **PIBT-1**, **PIBT-2**, **PIDS-2**, and **PI6F-2** anodes during GITT measurements. As illustrated in Figure 4e,f, the values of the Li^+ diffusion coefficient (D_{Li}) of **PIDS-2** and **PI6F-2** anodes were significantly higher than those of the **PIBT** series during the charge/discharge process. During the charging process (Figure 4e), **PI6F-2** exhibited a D_{Li} value of $\sim 1.3 \times 10^{-10}$ cm^2 s^{-1}, followed by **PIDS-2** ($\sim 1.1 \times 10^{-10}$ cm^2 s^{-1}), **PIBT-1** ($\sim 6.5 \times 10^{-11}$ cm^2 s^{-1}), and **PIBT-2** ($\sim 3.3 \times 10^{-11}$ cm^2 s^{-1}). This again indicated that bridge functionalization with electron-withdrawing groups enhances the Li^+ diffusivity during the charge/discharge process as the anode, which is consistent with the charge storage behavior. Furthermore, in the cases of **PIBT-1** and **PIBT-2** anodes, the isomerism also facilitates different diffusion pathways that affect Li^+ diffusivity, due to the different physical properties (surface area and degree of crystallinity).

In addition, the EIS measurement was again used at different temperatures to assess the activation energy of the TPPA-PI anodes. The relationship between the exchange current (i_0) and charge transfer resistance at electrode interfaces (R_{ct}) under different temperatures can be utilized to estimate the activation energies of active materials by using the Arrhenius equation, $i_0 = RT/nFR_{ct}$, and $i_0 = A \exp(-E_a/RT)$, where A represents the temperature-independent coefficient, R represents the gas constant, T represents the absolute temperature (K), n represents the number of transferred electrons, F represents the Faraday constant, and E_a represents the apparent activation energy.[60,61] Moreover, the activation energy can be calculated from $E_a = -Rk \ln 10$, where k is the slope of the fitting line of Arrhenius plots (Log_{10} i_0 as a function of 1000/T). Figure 5a–d shows the Nyquist plots of representative TPPA-PIs at different temperature ranges. Figure 5e shows the Log i_0 vs 1000/T plots of TPPA-PIs at different temperatures. The E_a's of TPPA-PI anodes were estimated to be 68.54, 67.39, 57.41, and 72.59 kJ mol^{-1} for **PIBT-1**, **PIBT-2**, **PIDS-2**, and **PI6F-2**, respectively (Figure 5f). Surprisingly, the E_a of TPPA-PI anodes with bridge functionalization on the imide units was significantly higher than those of our previous study (~30–40 kJ mol^{-1}).[31] This indicates that the bridge functionalization with electron-withdrawing groups on the imide unit significantly hindered the full utilization of Li^+ binding sites on the TPPA-PI anodes,

https://doi.org/10.1021/acsami.3c10722
ACS Appl. Mater. Interfaces XXXX, XXX, XXX–XXX

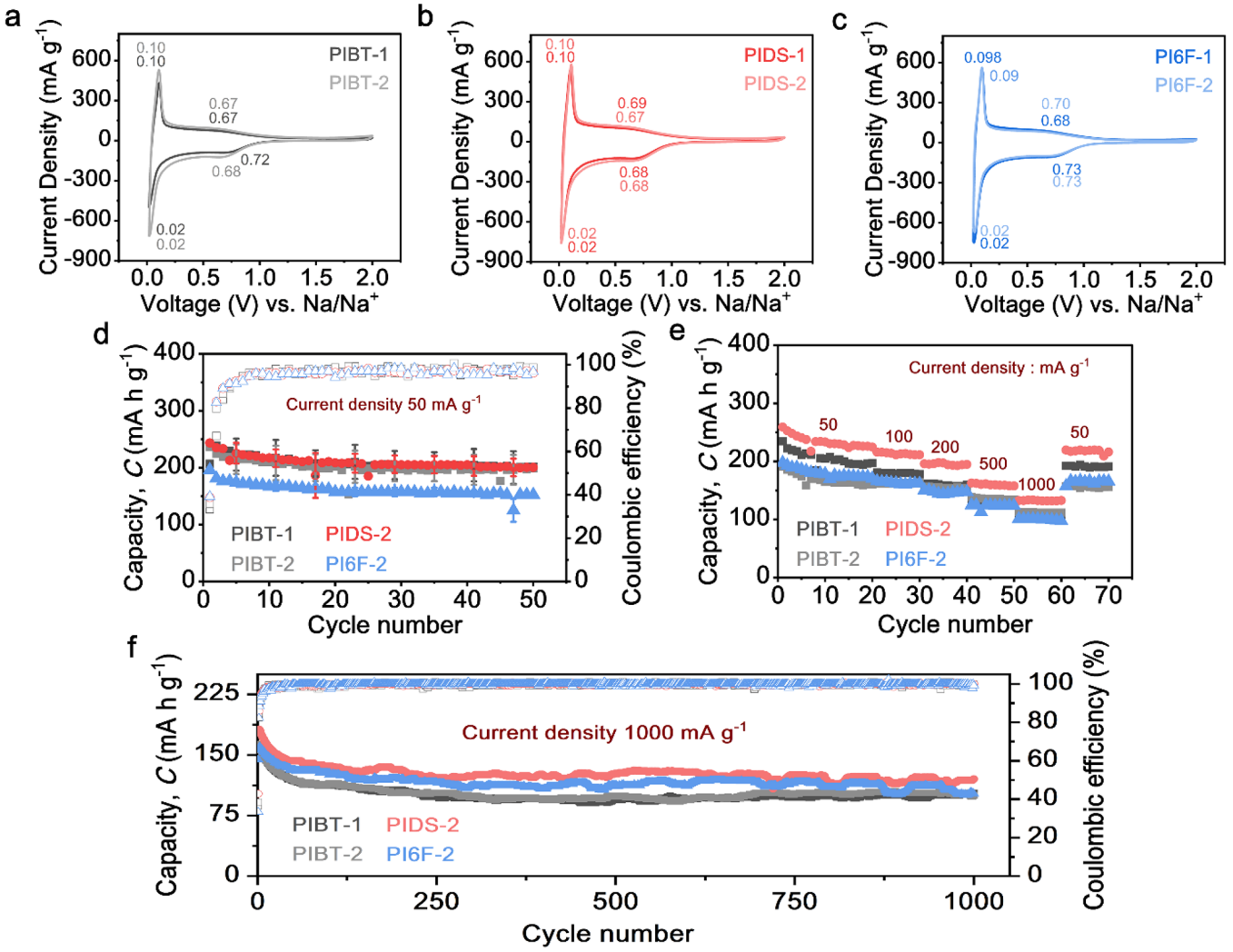

Figure 6. Electrochemical performance of TPPA-PI SiB anodes. (a–c) CV at the potential window of 0.02–2.0 V under 0.2 mV s^{-1}. (d) Capacity profile at 50 mA g^{-1} current density. (e) Rate performance. (f) Long cycling performance under a high current density of 1000 mA g^{-1}.

thus resulting in low capacity (Figure 3a). Furthermore, **PI6F-2** exhibited the highest E_a of 72.69 kJ mol^{-1}, higher than those of **PIDS-2**, **PIBT-1**, and **PIBT-2**, implying that extensive energy is required to promote the charge transfer reaction. This higher E_a of the **PI6F** series may have resulted from a greater charge polarization in the molecular structure due to $-CF_3$ bridge functionalization. This was in good agreement with the previous study that the charge polarization of fluorine electron-withdrawing character and the intramolecular hydrogen bonding will increase the activation energy.[57] Meanwhile, the E_a's of **PIBT-1** and **PIBT-2** were almost identical, implying that isomerism has little to no impact on the E_a in TPPA-PI anodes.

Battery Performance of TPPA-PIs as Sodium-Ion Battery (SiB) Anodes. The electrochemical performance of TPPA-PIs has been further elucidated to probe the capability as SiB anodes. Figure 6a–c shows the CVs of TPPA-PIs as SiB anodes. All TPPA-PI anodes showed identical behavior with two pairs of redox peaks at 0.67/0.72 and 0.02/0.10 V at a potential window of 0.02–2.0 V (vs Na/Na^+) under 0.2 mV s^{-1}, suggesting a successful insertion/deinsertion of Na^+ ions. This first pair of redox peaks at 0.67/0.72 V could be identified as the attachment/detachment process of Na ions onto carbonyl (C═O) and cyano groups of TPPA-PI anodes. Meanwhile, the second redox pair at 0.02/0.10 V was ascribed to Na^+ adsorption/desorption into carbonaceous groups.[62] Additionally, two well-defined plateaus can be monitored on the galvanostatic profiles of TPPA-PI SiB anodes (Figure S21), corresponding to the CV data (Figure 6a–c). However, significant capacity loss is monitored at the initial cycles, which could be attributed to the generation of SEI layers.[63]

Furthermore, the cycling performance of SiB anodes showed that **PIBT-1** delivered a specific capacity of 218 mA h g^{-1} after 50 cycles under 50 mA g^{-1}, followed by **PIBT-2**, **PIDS-2**, and **PI6F-2** with capacities of 205, 205, and 199 mA h g^{-1}, respectively. Meanwhile, the areal capacities of TPPA-PI SiB anodes were estimated as 13.952, 13.12, 13.12, and 12.736 mA h m^{-2} for **PIBT-1**, **PIBT-2**, **PIDS-2**, and **PI6F-2**, respectively (Table S4). Notably, these TPPA-PIs' performance as SiB anode was significantly lower than that as LiB anode (Figure 3a). This lower performance as SiB anode can be ascribed due to the larger cationic radius of Na^+ (1.02 Å) than that of Li^+ (0.76 Å) and the lowest binding energy to the given substrate than other alkali metals, which makes Na^+ less favorable for insertion in the sp^2 conjugated systems.[64−70] These limitations then hindered the Na^+ storage capability in the TPPA-PI anode for SiB, thus resulting in a significantly lower performance than that of as anode LiB. However, our TPPA-

https://doi.org/10.1021/acsami.3c10722
ACS Appl. Mater. Interfaces XXXX, XXX, XXX−XXX

PI performance is comparable with those of the reported polymeric-based SiB anodes (Table S8). The rate performance capability of SiB anodes was also evaluated and is depicted in Figure 6e. As shown in Figure 6e, **PIBT-1** anode delivered capacities of 205, 179, 159, 127, and 103 mA h g^{-1}, while **PIBT-2** displayed the specific capacities of 168, 162, 154, 135, and 112 mA h g^{-1} at current densities of 50, 100, 200, 500, and 1000 mA g^{-1}, respectively. The **PIDS-2** anode delivered capacities of 233, 213, 195, 159, and 132 mA h g^{-1}, while **PI6F-2** showed capacities of 179, 162, 146, 123, and 100 mA h g^{-1} at 50, 100, 200, 500, and 1000 mA g^{-1}, respectively. The excellent rate capability of SiB anodes was confirmed as their optimum capacities of 191, 156, 217, and 164 mA h g^{-1} could be recovered for **PIBT-1**, **PIBT-2**, **PIDS-2**, and **PI6F-2**, respectively, when the current density was switched back to 50 mA g^{-1}. Additionally, the stable long cycling performance under a relatively high current density (1000 mA g^{-1}) further confirmed the material stability of TPPA-PIs as SiB anode materials (Figure 6f). These electrochemical tests suggest that the TPPA-PIs could also be applied in next-generation multivalent energy storage devices.

CONCLUSION

In this work, we demonstrated three newly designed arylamine-based polyimides, TPPA-PIs, with three different bridge functionalizations on the imide units and their isomeric constituents, which can work as both cathodes and anodes for LiBs as well as SiB anodes. As LiB cathode, a maximum energy density of ∼250 Wh kg^{-1} with high voltage operation can be obtained for TPPA-PIs. As the anode, the TPPA-PIs showed a reversible storage capacity of ∼800 mA h g^{-1} at 100 mA g^{-1} via a superlithiation process and demonstrated good rate capability up to a current density of 2000 mA g^{-1}. Notably, a higher conductive carbon is necessary for TPPA-PI anodes to provide a high conductive environment; thus superlithiation could be facilitated. Moreover, when applied as SiB anode, TPPA-PI delivered an optimum specific capacity of 218 mA h g^{-1} after 50 cycles at 50 mA g^{-1} and had a long cycling stability up to 1000 cycles under a high current density of 1000 mA g^{-1}. The mechanistic studies show that both bridge functionalization on the imide units and isomerism impact the electrochemical performance of TPPA-PIs by regulating their intrinsic properties such as charge storage behavior, ion diffusivity, and activation energy. This study paves the way for the strategically structural design of polymeric electrodes for next-generation organic batteries.

EXPERIMENTAL SECTION

Materials. *N*,*N*-Bis(4-nitrophenyl)-*N*′,*N*′-di(4-cyanophenyl)-1,4-phenylenediamine (**1**) and *N*,*N*′-bis(4-aminophenyl)-*N*,*N*′-di(4-cyanophenyl)-1,4-phenylenediamine (**2**) were synthesized according to a previously reported procedure.[27] Commercially available aromatic tetracarboxylic dianhydrides such as 3,3′,4,4′-benzophenonetetracarboxylic dianhydride (**3-BT**; Chriskev) and 3,3′,4,4′-diphenylsulfonetetracarboxylic dianhydride (**3-DS**; TCI) were purified by recrystallization from acetic anhydride. 2,2-Bis(3,4-dicarboxyphenyl)-hexafluoropropane dianhydride (**3-6F**; Chriskev) was purified by vacuum sublimation. Carbon black, conductive carbon (Super P; >99% (metal basis)), polyvinylidene fluoride (PVDF; Alfa Aesar), NMP (>99%, Thermo Fisher Scientific), ethylene carbonate (EC; >99%, Alfa Aesar), diethyl carbonate (DEC; >99%, Acros Organic), and sodium perchlorate ($NaClO_4$; anhydrous, Alfa Aesar) were used. Lithium hexafluorophosphate ($LiPF_6$), 1 M, in EC and DEC (1:1 v/v) was purchased from UBIQ Technology Co., Ltd. All chemicals were used as received without further purification unless specified.

Preparation of Polyimides by Two-Step Method via Chemical Imidization Reaction. The synthesis of PI **PIBT-1** was used as an example to illustrate the general synthetic route. To a solution of 1.97 g (4.00 mmol) of diamine **1** in 13.0 mL of NMP, 1.29 g (4.00 mmol) of dianhydride **3-BT** was added in one portion. The mixture was stirred at room temperature overnight (*ca.* 12 h) to afford a viscous poly(amic acid) solution. The poly(amic acid) was subsequently converted to PI via a chemical imidization process by the addition of 8 mL of pyridine and 14 mL of acetic anhydride, and then the mixture was heated at 120 °C for 4 h to effect complete imidization. The resulting polymer solution was poured into 300 mL of methanol, giving a fibrous precipitate, which was washed thoroughly with methanol and collected by filtration. The inherent viscosity and weight-average molecular weight (M_w) of **PIBT-1** were 1.04 dL/g (measured at a concentration of 0.5 g/dL in DMAc at 30 °C) and 84 400 Da, respectively. The FT-IR spectrum of **PIBT-1** (film) exhibited characteristic absorption bands at 2222 cm^{-1} (C≡N stretch), 1723−1676 cm^{-1} (asymmetric C═O stretch), and 1611−1595 cm^{-1} (symmetric C═O stretch). ^1H NMR (500 MHz, $CDCl_3$, δ, ppm): 7.06 (d, J = 8.6 Hz, 2H, H_f), 7.15 (d, J = 8.5 Hz, 4H, H_h), 7.20 (d, J = 7.85 Hz, 2H, H_g), 7.29 (d, J = 8.4 Hz, 4H, H_e), 7.40 (d, J = 8.2 Hz, 4H, H_e), 7.55 (d, J = 8.25 Hz, 4H, H_i), 8.16 (d, J = 7.5 Hz, 2H, H_c), 8.29 (m, 4H, H_a + H_b). ^{13}C NMR (125 MHz, $CDCl_3$, δ, ppm): 105.87 (C^{20}), 118.92 (−C≡N, C^{21}), 122.83 (C^{18}), 124.42 (C^5), 124.47 (C^{11}), 124.77 (C^4), 126.20 (C^{15}), 127.58 (C^{10}), 128.03 (C^{14}), 132.16 (C^6), 133.66 (C^{19}), 135.04 (C^7), 135.91 (C^3), 140.37 (C^{12}), 141.94 (C^{13}), 145.00 (C^9), 146.83 (C^{16}), 150.07 (C^{17}), 166.20 (C^2), 166.22 (imide ring carbonyl, C^8), 192.81 (benzophenone-carbonyl, C^1). Anal. Calcd (%) for $(C_{49}H_{26}N_6O_5)_n$: C, 75.57%; H, 3.37%; N, 10.79%. Found: C, 71.72%; H, 4.10%; N, 10.74%. The other PIs were prepared by an analogous procedure.

Model Compound Synthesis (Scheme S1). *Synthesis of BTDA-Based Diimide Model Compound (**BTDA2+**).* A mixture of 3.64 g (11.29 mmol) of dianhydride **3-BT**, 4.31 g (2.55 equiv, 28.88 mmol) of monoamine 4-*tert*-butylaniline, and 30 mL of acetic acid was heated with constant stirring at 140 °C for 12 h. The resulting precipitate was filtered and washed by 100 mL of stirring methanol. The product was collected by filtration and dried to obtain a white powder with a quantitative yield. ^1H NMR (500 MHz, $CDCl_3$, δ, ppm): 1.37 (s, 18H), 7.38 (d, J = 7.63 Hz, 4H), 7.55 (d, J = 7.65 Hz, 4H), 8.15 (d, J = 7.53 Hz, 2H), 8.27 (d, J = 7.68 Hz, 2H), 8.29 (s, 2H).

*Synthesis of DSDA-Based Diimide Model Compound (**DSDA2+**).* A mixture of 3.27 g (9.13 mmol) of dianhydride **3-DS**, 3.49 g (2.56 equiv, 23.39 mmol) of monoamine 4-*tert*-butylaniline, and 6 mL of acetic acid was heated with constant stirring at 140 °C for 12 h. The resulting precipitate was filtered and washed by 100 mL of stirring methanol. The product was collected by filtration and dried to obtain a light brown powder with a quantitative yield. ^1H NMR (500 MHz, $CDCl_3$, δ, ppm): 1.35 (s, 18H), 7.32 (d, J = 8.55 Hz, 4H), 7.53 (d, J = 8.60 Hz, 4H), 8.15 (d, J = 7.75 Hz, 2H), 8.46 (d, J = 7.80 Hz, 2H), 8.52 (s, 2H).

*Synthesis of 6FDA-Based Diimide Model Compound (**6FDA2+**).* A mixture of 3.01 g (6.77 mmol) of dianhydride **3-6F**, 2.57 g (2.54 equiv, 17.22 mmol) of monoamine 4-*tert*-butylaniline, and 6 mL of acetic acid was heated with constant stirring at 140 °C for 12 h. The resulting precipitate was filtered and washed by 100 mL of stirring methanol. The resulting mixture was poured into 50 mL of stirring water. The precipitate was collected by filtration, washed thoroughly with water, and dried to obtain a white powder with a quantitative yield. ^1H NMR (500 MHz, $CDCl_3$, δ, ppm): 1.36 (s, 18H), 7.34 (d, J = 8.60 Hz, 4H), 7.54 (d, J = 8.60 Hz, 4H), 7.88 (d, J = 8.05 Hz, 2H), 7.93 (s, 2H), 8.04 (d, J = 8.05 Hz, 2H).

Material Characterization. Molecular weights are measured by gel permeation chromatographic (GPC) analysis on a Waters chromatographic unit interfaced with a Waters 2410 refractive index detector. Two Shodex GPC KD-803 and GPC KD-804 were connected in series with NMP and LiCl salt (20 mM) as the eluent

https://doi.org/10.1021/acsami.3c10722
ACS Appl. Mater. Interfaces XXXX, XXX, XXX−XXX

at a flow rate of 0.35 mL/min at 40 °C and were calibrated with polystyrene standards. Elemental analyses (C, H, and N) were recorded on an Elementar vario EL cube elemental analyzer. Fourier transform infrared (FT-IR) spectra were recorded on PerkinElmer Spectrum 100 Model FT-IR and JASCO FT/IR-6600 spectrometers. NMR spectra were measured on a Bruker AVANCE-500 FT-NMR using tetramethylsilane as an internal reference, and peak multiplicity was reported as follows: s, singlet; d, doublet; m, multiplet. The inherent viscosities were determined at 0.5 g/dL concentration with a Tamson TV-2000 viscometer at 30 °C. TGA was conducted with a PerkinElmer Pyris 1 TGA. Experiments were carried out on approximately 6−8 mg film samples heated in flowing nitrogen or air (flow rate = 20 cm^3/min) at a heating rate of 20 °C/min. DSC analyses were performed on a PerkinElmer Pyris 1 DSC at a scan rate of 10 °C/min in flowing nitrogen (20 cm^3/min). The nitrogen adsorption isotherms were measured at 77 K with an accelerated surface area and porosimetry system, ASAP 2020 (Micromeritics, Norcross, GA). Prior to the nitrogen adsorption isotherm measurements the samples were degassed at 120 °C for 6 h. The X-ray diffraction spectra were measured on a Bruker D8 Advance X-ray diffractometer at 40 kV and 40 mA using Cu Kα radiation (λ = 1.5406 Å).

■ ASSOCIATED CONTENT

Supporting Information

The Supporting Information is available free of charge at https://pubs.acs.org/doi/10.1021/acsami.3c10722.

Supplementary notes; model compound synthesis; FT-IR, NMR, and XRD spectra; N_2 adsorption−desorption; cyclic voltammogram; galvanostatic profile; Nyquist plots; sweep rate analysis; GITT profile; capacity profile; supplementary tables (PDF)

■ AUTHOR INFORMATION

Corresponding Authors

Hung-Ju Yen − *Institute of Chemistry, Academia Sinica, Taipei 11529, Taiwan;* orcid.org/0000-0002-6316-9124; Email: hjyen@gate.sinica.edu.tw

Guey-Sheng Liou − *Institute of Polymer Science and Engineering, National Taiwan University, Taipei 10617, Taiwan;* orcid.org/0000-0003-3725-3768; Email: gsliou@ntu.edu.tw

Authors

Andre Lammiduk Lubis − *Institute of Chemistry, Academia Sinica, Taipei 11529, Taiwan; Sustainable Chemical Science and Technology Program, Taiwan International Graduate Program (TIGP), Academia Sinica and National Taiwan University, Taipei 11529, Taiwan; Department of Chemical Engineering, National Taiwan University, Taipei 10617, Taiwan*

Febri Baskoro − *Institute of Chemistry, Academia Sinica, Taipei 11529, Taiwan;* orcid.org/0000-0001-8408-6726

Ting-Hsuan Lin − *Institute of Chemistry, Academia Sinica, Taipei 11529, Taiwan; Department of Chemical Engineering, National Taiwan University of Science and Technology, Taipei 106, Taiwan*

Hui Qi Wong − *Institute of Chemistry, Academia Sinica, Taipei 11529, Taiwan; Sustainable Chemical Science and Technology Program, Taiwan International Graduate Program (TIGP), Academia Sinica and National Taiwan University, Taipei 11529, Taiwan; Department of Chemical Engineering, National Taiwan University, Taipei 10617, Taiwan*

Complete contact information is available at: https://pubs.acs.org/10.1021/acsami.3c10722

Author Contributions

A.L.L. and F.B. contributed equally. The manuscript was written through the contributions of all authors. All authors have approved the final version of the manuscript.

Notes

The authors declare no competing financial interest.

■ ACKNOWLEDGMENTS

F.B. acknowledges the postdoctoral fellowship program supported by Academia Sinica (AS-PD-11201-M04). H.-J.Y. acknowledges the financial support by Innovative Materials and Analysis Technology Exploration in Academia Sinica (AS-iMATE-111-21) and the Ministry of Science and Technology in Taiwan (MOST 111-2124-M-001-001; NSTC 111-2113-M-001-051). The authors also gratefully acknowledge the support of elemental analysis by Ching-Wei Lu in the Precision Instrumentation Center, National Taiwan University (MOST EA0002).

■ REFERENCES

(1) Long, L.; Wang, S.; Xiao, M.; Meng, Y. Polymer electrolytes for lithium polymer batteries. *J. Mater. Chem. A* **2016**, *4* (26), 10038−10069.

(2) Dunn, B.; Kamath, H.; Tarascon, J.-M. Electrical Energy Storage for the Grid: A Battery of Choices. *Science* **2011**, *334* (6058), 928.

(3) Tarascon, J. M.; Armand, M. Issues and challenges facing rechargeable lithium batteries. *Nature* **2001**, *414*, 359.

(4) Bruce, P. G.; Scrosati, B.; Tarascon, J.-M. Nanomaterials for Rechargeable Lithium Batteries. *Angew. Chem., Int. Ed.* **2008**, *47* (16), 2930−2946.

(5) Goodenough, J. B.; Kim, Y. Challenges for rechargeable Li batteries. *Chem. Mater.* **2010**, *22* (3), 587−603.

(6) Li, K.; Xu, S.; Han, D.; Si, Z.; Wang, H. G. Carbonyl-rich Poly(pyrene-4,5,9,10-tetraone Sulfide) as Anode Materials for High-Performance Li and Na-Ion Batteries. *Chem.—Asian J.* **2021**, *16* (14), 1973−1978.

(7) Rohland, P.; Schröter, E.; Nolte, O.; Newkome, G. R.; Hager, M. D.; Schubert, U. S. Redox-active polymers: The magic key towards energy storage - a polymer design guideline progress in polymer science. *Prog. Polym. Sci.* **2022**, *125*, 101474.

(8) Liu, K.; Liu, Y.; Lin, D.; Pei, A.; Cui, Y. Materials for lithium-ion battery safety. *Sci. Adv.* **2018**, *4* (6), No. eaas9820.

(9) Liu, C.; Neale, Z. G.; Cao, G. Understanding electrochemical potentials of cathode materials in rechargeable batteries. *Mater. Today* **2016**, *19* (2), 109−123.

(10) Manthiram, A. A reflection on lithium-ion battery cathode chemistry. *Nat. Commun.* **2020**, *11* (1), 1550.

(11) Man, Z.; Li, P.; Zhou, D.; Zang, R.; Wang, S.; Li, P.; Liu, S.; Li, X.; Wu, Y.; Liang, X.; Wang, G. High-performance lithium-organic batteries by achieving 16 lithium storage in poly(imine-anthraquinone). *J. Mater. Chem. A* **2019**, *7* (5), 2368−2375.

(12) Larcher, D.; Tarascon, J. M. Towards greener and more sustainable batteries for electrical energy storage. *Nat. Chem.* **2015**, *7* (1), 19−29.

(13) Poizot, P.; Dolhem, F. Clean energy new deal for a sustainable world: from non-CO_2 generating energy sources to greener electrochemical storage devices. *Energy Environ. Sci.* **2011**, *4* (6), 2003−2019.

(14) Lee, S.; Kwon, G.; Ku, K.; Yoon, K.; Jung, S.-K.; Lim, H.-D.; Kang, K. Recent Progress in Organic Electrodes for Li and Na Rechargeable Batteries. *Adv. Mater.* **2018**, *30* (42), 1704682.

(15) Tong, Z.; Tian, S.; Wang, H.; Shen, D.; Yang, R.; Lee, C.-S. Tailored Redox Kinetics, Electronic Structures and Electrode/

Electrolyte Interfaces for Fast and High Energy-Density Potassium-Organic Battery. *Adv. Funct. Mater.* **2020**, *30* (5), 1907656.
(16) Gannett, C. N.; Kim, J.; Tirtariyadi, D.; Milner, P. J.; Abruña, H. D. Investigation of ion-electrode interactions of linear polyimides and alkali metal ions for next generation alternative-ion batteries. *Chem. Sci.* **2022**, *13* (32), 9191−9201.
(17) Shestakov, A. F.; Yarmolenko, O. V.; Ignatova, A. A.; Mumyatov, A. V.; Stevenson, K. J.; Troshin, P. A. Structural origins of capacity fading in lithium-polyimide batteries. *J. Mater. Chem. A* **2017**, *5* (14), 6532−6537.
(18) Kim, J.; Shirke, Y.; Milner, P. J. Flexible Backbone Effects on the Redox Properties of Perylenediimide-Based Polymers. *ACS Appl. Mater. Interfaces* **2023**, DOI: 10.1021/acsami.3c06065.
(19) Zhang, Q.; Cui, X.; Hao, S.; Zhang, Q.; Guo, Z.; Li, H.; Lin, Z.; Yang, Y. Chain engineering of carbonyl polymers for sustainable lithium-ion batteries. *Mater. Today* **2021**, *50*, 170−198.
(20) Zhang, Q.; Dou, Y.; He, Q.; Deng, S.; Huang, Q.; Huang, S.; Yang, Y. Emerging Carbonyl Polymers as Sustainable Electrode Materials for Lithium-Free Metal-Ion Batteries. *Energy Environ. Mater.* **2022**, *5* (4), 1037−1059.
(21) Song, Z.; Zhan, H.; Zhou, Y. Polyimides: Promising Energy-Storage Materials. *Angew. Chem., Int. Ed.* **2010**, *49* (45), 8444−8448.
(22) Wang, H.; Yao, C.-J.; Nie, H.-J.; Wang, K.-Z.; Zhong, Y.-W.; Chen, P.; Mei, S.; Zhang, Q. Recent progress in carbonyl-based organic polymers as promising electrode materials for lithium-ion batteries (LIBs). *J. Mater. Chem. A* **2020**, *8* (24), 11906−11922.
(23) Wang, J.; Liu, H.; Du, C.; Zhang, X.; Liu, Y.; Yao, H.; Sun, Z.; Guan, S. Conjugated diketone-linked polyimide cathode material for organic lithium-ion batteries. *Chem. Eng. J.* **2022**, *444*, 136598.
(24) Lu, Y.; Zhang, Q.; Li, L.; Niu, Z.; Chen, J. Design Strategies toward Enhancing the Performance of Organic Electrode Materials in Metal-Ion Batteries. *Chem.* **2018**, *4* (12), 2786−2813.
(25) Oubaha, H.; Gohy, J.-F.; Melinte, S. Carbonyl-Based π-Conjugated Materials: From Synthesis to Applications in Lithium-Ion Batteries. *ChemPlusChem.* **2019**, *84* (9), 1179−1214.
(26) Lyu, H.; Sun, X.-G.; Dai, S. Organic Cathode Materials for Lithium-Ion Batteries: Past, Present, and Future. *Adv. Energy Sustainability Res.* **2021**, *2* (1), 2000044.
(27) Du, W.; Du, X.; Ma, M.; Huang, S.; Sun, X.; Xiong, L. Polymer Electrode Materials for Lithium-Ion Batteries. *Adv. Funct. Mater.* **2022**, *32* (21), 2110871.
(28) Han, X.; Chang, C.; Yuan, L.; Sun, T.; Sun, J. Aromatic Carbonyl Derivative Polymers as High-Performance Li-Ion Storage Materials. *Adv. Mater.* **2007**, *19* (12), 1616−1621.
(29) Kim, J.; Kim, J. H.; Ariga, K. Redox-Active Polymers for Energy Storage Nanoarchitectonics. *Joule* **2017**, *1* (4), 739−768.
(30) Labasan, K. B.; Lin, H.-J.; Baskoro, F.; Togonon, J. J. H.; Wong, H. Q.; Chang, C.-W.; Arco, S. D.; Yen, H.-J. Dicyanotriphenylamine-Based Polyimides as High-Performance Electrodes for Next Generation Organic Lithium-Ion Batteries. *ACS Appl. Mater. Interfaces* **2021**, *13* (15), 17467−17477.
(31) Baskoro, F.; Lubis, A. L.; Wong, H. Q.; Liou, G.-S.; Yen, H.-J. Redox-active polynaphthalimides as versatile electrode materials for high-voltage, high-rate and long-cycle-life organic Li-ion batteries. *J. Mater. Chem. A* **2023**, *11* (21), 11210−11221.
(32) Zhang, Q.; Lin, G.; He, Y.; Cui, X.; Yang, Y. Chain engineering-tailored microstructures and lithium storage performance of hydrothermally-synthesized linear polyimides. *Mater. Today Chem.* **2020**, *17*, 100341.
(33) Zhang, X.; Cui, X.; Lu, C.-H.; Li, H.; Zhang, Q.; He, C.; Yang, Y. Conjugated polyimide-coated carbon nanofiber aerogels in a redox electrolyte for binder-free supercapacitors. *Chem. Eng. J.* **2020**, *401*, 126031.
(34) Li, M.; Lu, J.; Chen, Z.; Amine, K. 30 Years of Lithium-Ion Batteries. *Adv. Mater.* **2018**, *30* (33), 1800561.
(35) He, J.; Liao, Y.; Hu, Q.; Zeng, Z.; Yi, L.; Wang, Y.; Lu, H.; Pan, M. Investigation of polyimide as an anode material for lithium-ion battery and its thermal safety behavior. *Ionics* **2020**, *26* (7), 3343−3350.
(36) Zhang, C.; Chen, S.; Zhou, G.; Hou, Q.; Luo, S.; Wang, Y.; Shi, G. Poly(arylamine-imide)s Cathode Materials for Lithium-Ion Batteries with High Average Voltage and Long Cycle Life. *J. Electrochem. Soc.* **2021**, *168* (5), 050548.
(37) Liu, H.; Wang, Y.; Liu, H.; Sun, Y.; Guan, S. Homology and isomerism effect of aromatic imides as organic anode materials of lithium-ion batteries. *J. Electroanal. Chem.* **2019**, *848*, 113289.
(38) Huang, W.; Jia, T.; Zhou, G.; Chen, S.; Hou, Q.; Wang, Y.; Luo, S.; Shi, G.; Xu, B. A triphenylamine-based polymer with anthraquinone side chain as cathode material in lithium ion batteries. *Electrochim. Acta* **2018**, *283*, 1284−1290.
(39) Su, C.; Yang, F.; Ji, L.; Xu, L.; Zhang, C. Polytriphenylamine derivative with high free radical density as the novel organic cathode for lithium ion batteries. *J. Mater. Chem. A* **2014**, *2* (47), 20083−20088.
(40) Feng, J. K.; Cao, Y. L.; Ai, X. P.; Yang, H. X. Polytriphenylamine: A high power and high capacity cathode material for rechargeable lithium batteries. *J. Power Sources* **2008**, *177* (1), 199−204.
(41) Zhang, C.; Yang, X.; Ren, W.; Wang, Y.; Su, F.; Jiang, J.-X. Microporous organic polymer-based lithium ion batteries with improved rate performance and energy density. *J. Power Sources* **2016**, *317*, 49−56.
(42) Xu, T.; Xiong, J.; Du, X.; Zhang, Y.; Song, S.; Xiong, C.; Dong, L. Polytriphenylamine Derivative and Carbon Nanotubes as Cathode Materials for High-Performance Polymer-Based Batteries. *J. Phys. Chem. C* **2018**, *122* (35), 20057−20063.
(43) Su, C.; He, H.; Xu, L.; Zhao, K.; Zheng, C.; Zhang, C. A mesoporous conjugated polymer based on a high free radical density polytriphenylamine derivative: its preparation and electrochemical performance as a cathode material for Li-ion batteries. *J. Mater. Chem. A* **2017**, *5* (6), 2701−2709.
(44) Su, C.; Ji, L.; Xu, L.; Zhou, N.; Wang, G.; Zhang, C. A polytriphenylamine derivative exhibiting a four-electron redox center as a high free radical density organic cathode. *RSC Adv.* **2016**, *6* (27), 22989−22995.
(45) Su, C.; Yang, F.; Ji, L.; Xu, L.; Zhang, C. Polytriphenylamine derivative with high free radical density as the novel organic cathode for lithium ion batteries. *J. Mater. Chem. A* **2014**, *2* (47), 20083−20088.
(46) Kang, H.; Liu, H.; Li, C.; Sun, L.; Zhang, C.; Gao, H.; Yin, J.; Yang, B.; You, Y.; Jiang, K.-C.; Long, H.; Xin, S. Polyanthraquinone-Triazine—A Promising Anode Material for High-Energy Lithium-Ion Batteries. *ACS Appl. Mater. Interfaces* **2018**, *10* (43), 37023−37030.
(47) Wu, J.; Rui, X.; Wang, C.; Pei, W.-B.; Lau, R.; Yan, Q.; Zhang, Q. Nanostructured Conjugated Ladder Polymers for Stable and Fast Lithium Storage Anodes with High-Capacity. *Adv. Energy Mater.* **2015**, *5* (9), 1402189.
(48) Zawadzka, M.; Nitschke, P.; Musioł, M.; Siwy, M.; Pluczyk-Małek, S.; Honisz, D.; Łapkowski, M. Naphthalene Phthalimide Derivatives as Model Compounds for Electrochromic Materials. *Molecules* **2023**, *28* (4), 1740.
(49) Renault, S.; Oltean, V. A.; Araujo, C. M.; Grigoriev, A.; Edström, K.; Brandell, D. Superlithiation of Organic Electrode Materials: The Case of Dilithium Benzenedipropiolate. *Chem. Mater.* **2016**, *28* (6), 1920−1926.
(50) McAllister, B. T.; Grignon, E.; Schon, T. B.; An, S. Y.; Yim, C.-H.; Abu-Lebdeh, Y.; Seferos, D. S. High-Rate Activation of Organic Superlithiation Anodes. *ACS Appl. Energy Mater.* **2021**, *4* (7), 6659−6666.
(51) Lei, Z.; Chen, X.; Sun, W.; Zhang, Y.; Wang, Y. Exfoliated Triazine-Based Covalent Organic Nanosheets with Multielectron Redox for High-Performance Lithium Organic Batteries. *Adv. Energy Mater.* **2019**, *9* (3), 1801010.
(52) Zhao, X.; Du, Y.; Jin, L.; Yang, Y.; Wu, S.; Li, W.; Yu, Y.; Zhu, Y.; Zhang, Q. Membranes of MnO Beading in Carbon Nanofibers as Flexible Anodes for High-Performance Lithium-Ion Batteries. *Sci. Rep.* **2015**, *5* (1), 14146.

https://doi.org/10.1021/acsami.3c10722
ACS Appl. Mater. Interfaces XXXX, XXX, XXX−XXX

(53) Molina, A.; Patil, N.; Ventosa, E.; Liras, M.; Palma, J.; Marcilla, R. Electrode Engineering of Redox-Active Conjugated Microporous Polymers for Ultra-High Areal Capacity Organic Batteries. *ACS Energy Lett.* **2020**, *5* (9), 2945−2953.
(54) Yang, H.; Liu, S.; Cao, L.; Jiang, S.; Hou, H. Superlithiation of non-conductive polyimide toward high-performance lithium-ion batteries. *J. Mater. Chem. A* **2018**, *6* (42), 21216−21224.
(55) Schon, T. B.; An, S. Y.; Tilley, A. J.; Seferos, D. S. Unusual Capacity Increases with Cycling for Ladder-Type Microporous Polymers. *ACS Appl. Mater. Interfaces* **2019**, *11* (2), 1739−1747.
(56) Han, X.; Qing, G.; Sun, J.; Sun, T. How Many Lithium Ions Can Be Inserted onto Fused C_6 Aromatic Ring Systems? *Angew. Chem., Int. Ed.* **2012**, *51* (21), 5147−5151.
(57) Baskoro, F.; Lin, H.-J.; Chang, C.-W.; Wang, C.-L.; Lubis, A. L.; Yen, H.-J. High-performance aramid electrodes for high-rate and long cycle-life organic Li-ion batteries. *J. Mater. Chem. A* **2023**, *11* (2), 569−578.
(58) Li, J.; Luo, M.; Ba, Z.; Wang, Z.; Chen, L.; Li, Y.; Li, M.; Li, H.-B.; Dong, J.; Zhao, X.; Zhang, Q. Hierarchical multicarbonyl polyimide architectures as promising anode active materials for high-performance lithium/sodium ion batteries. *J. Mater. Chem. A* **2019**, *7* (32), 19112−19119.
(59) Baskoro, F.; Ngue, C.-M.; Labasan, K. B.; Wong, H. Q.; Leung, M.-K.; Yen, H.-J. Dual-Ligand Zn-Based Metal-Organic Framework as Reversible and Stable Anode Material for Next Generation Lithium-Ion Batteries. *Energy Technol.* **2021**, *9* (11), 2100212.
(60) Yamada, I.; Iriyama, Y.; Abe, T.; Ogumi, Z. Lithium-ion transfer on a Li_xCoO_2 thin film electrode prepared by pulsed laser deposition—Effect of orientation. *J. Power Sources* **2007**, *172*, 933−937.
(61) Xu, J.; Jeon, I.-Y.; Seo, J.-M.; Dou, S.; Dai, L.; Baek, J.-B. Edge-Selectively Halogenated Graphene Nanoplatelets (XGnPs, X = Cl, Br, or I) Prepared by Ball-Milling and Used as Anode Materials for Lithium-Ion Batteries. *Adv. Mater.* **2014**, *26* (43), 7317−7323.
(62) Park, Y.; Shin, D.-S.; Woo, S. H.; Choi, N. S.; Shin, K. H.; Oh, S. M.; Lee, K. T.; Hong, S. Y. Sodium Terephthalate as an Organic Anode Material for Sodium Ion Batteries. *Adv. Mater.* **2012**, *24* (26), 3562−3567.
(63) Armand, M.; Grugeon, S.; Vezin, H.; Laruelle, S.; Ribière, P.; Poizot, P.; Tarascon, J. M. Conjugated dicarboxylate anodes for Li-ion batteries. *Nat. Mater.* **2009**, *8* (2), 120−125.
(64) Kang, H.; Liu, Y.; Cao, K.; Zhao, Y.; Jiao, L.; Wang, Y.; Yuan, H. Update on anode materials for Na-ion batteries. *J. Mater. Chem. A* **2015**, *3* (35), 17899−17913.
(65) Jache, B.; Adelhelm, P. Use of Graphite as a Highly Reversible Electrode with Superior Cycle Life for Sodium-Ion Batteries by Making Use of Co-Intercalation Phenomena. *Angew. Chem., Int. Ed.* **2014**, *53* (38), 10169−10173.
(66) Wen, Y.; He, K.; Zhu, Y.; Han, F.; Xu, Y.; Matsuda, I.; Ishii, Y.; Cumings, J.; Wang, C. Expanded graphite as superior anode for sodium-ion batteries. *Nat. Commun.* **2014**, *5* (1), 4033.
(67) Cao, Y.; Xiao, L.; Sushko, M. L.; Wang, W.; Schwenzer, B.; Xiao, J.; Nie, Z.; Saraf, L. V.; Yang, Z.; Liu, J. Sodium Ion Insertion in Hollow Carbon Nanowires for Battery Applications. *Nano Lett.* **2012**, *12* (7), 3783−3787.
(68) Chayambuka, K.; Mulder, G.; Danilov, D. L.; Notten, P. H. L. Sodium-Ion Battery Materials and Electrochemical Properties Reviewed. *Adv. Energy Mater.* **2018**, *8* (16), 1800079.
(69) Liu, Y.; Merinov, B. V.; Goddard, W. A. Origin of low sodium capacity in graphite and generally weak substrate binding of Na and Mg among alkali and alkaline earth metals. *Proc. Nat. Acad. Sci.* **2016**, *113* (14), 3735−3739.
(70) Nobuhara, K.; Nakayama, H.; Nose, M.; Nakanishi, S.; Iba, H. First-principles study of alkali metal-graphite intercalation compounds. *J. Power Sources* **2013**, *243*, 585−587.

https://doi.org/10.1021/acsami.3c10722
ACS Appl. Mater. Interfaces XXXX, XXX, XXX−XXX